Advances in Geo-Energy Research

Vol. 9, No. 2, p. 106-116, 2023

Original article

Pseudopotential-based multiple-relaxation-time lattice Boltzmann model for multicomponent and multiphase slip flow

Wendong Wang[1,2], Qiuheng Xie[1,2], Han Wang[3]*, Yuliang Su[1,2], Sina Rezaei-Gomari[4]

[1]*Key Laboratory of Unconventional Oil & Gas Development, China University of Petroleum (East China), Ministry of Education, Qingdao 266580, P. R. China*

[2]*School of Petroleum Engineering, China University of Petroleum (East China), Qingdao 266580, P. R. China*

[3]*State Key Laboratory of Petroleum Resources and Prospecting, China University of Petroleum, Beijing 102249, P. R. China*

[4]*School of Computing, Engineering and Digital Technologies, Teesside University, Middlesbrough, TS1-3BX, UK*

Keywords:
Slip boundary
multiphase flow
lattice Boltzmann method
combination parameter
diffusive Maxwell's reflection

Cited as:
Wang, W., Xie, Q., Wang, H., Su, Y., Rezaei-Gomari, S. Pseudopotential-based multiple-relaxation-time lattice Boltzmann model for multicomponent and multiphase slip flow. Advances in Geo-Energy Research, 2023, 9(2): 106-116.
https://doi.org/10.46690/ager.2023.08.04

Abstract:
The microscale liquid flow in nanoscale systems considering slip boundary has been widely studied in recent years, however, they are limited to single-phase flow. As in nature, multicomponent and multiphase flows can also exist with non-zero slip velocities, such as oil/water slip flow in nanoporous shale. In this paper, a novel multicomponent-multiphase multiple-relaxation-time lattice Boltzmann method with a combinational slip boundary condition is developed to study the two-phase slip flow behaviors. The proposed combined slip boundary condition is derived from adjustments to the conventional diffusive Maxwell's reflection and half-way bounce-back scheme boundary parameters, incorporating a compelled conservation requirement. With the analysis of simulations for the layer, slug, and droplet types of two-phase flow in single pores, and two-phase flow in porous media with complex wall geometry, it can be concluded that the proposed schemes of two-phase slip boundary conditions are particularly suitable for multicomponent and multiphase flow with a non-zero slip velocity. The proposed model can be used to determine relative permeability and simulate spontaneous imbibition in particular in shale reservoirs where those flow properties are hard-to-determine.

1. Introduction

Boundary slip is a crucial phenomenon governing liquid flow in nanoscale environments. A comprehensive comprehension of confined liquid flow behaviors within such spaces holds significant scientific and practical significance, encompassing applications in shale reservoirs (Zhang et al., 2018; Seyyedattar et al., 2019; Zhang et al., 2020; Ham et al., 2022), water purification (Das et al., 2014), catalysis in fuel cells (Shin et al., 2018), biochemical nanosensors (Cui et al., 2001) and drug delivery across biological cell membranes (Gravelle et al., 2013; Geng et al., 2014). While liquid flow within a single pore can be described using a conventional no-slip continuity equation, in nanopores, the presence of slip boundary can lead to actual flow rates of confined liquid that are potentially a hundredfold greater than those predicted by the no-slip Hagen-Poiseuille (HP) equation (Wu et al., 2017). Moreover, the conventional equation can not accurately capture the complex boundary conditions of fluid flow in the nanoporous medium (Feng et al., 2020).

Over the past decade, numerous researchers have conducted theoretical analyses to investigate the flow behaviors of single-phase fluids in nanoscale environments. Mattia and Calabrò (2012) adapted the HP equation to incorporate solid-liquid interactions, enabling the exploration of confined water flow within carbon nanotubes. Their study encompassed an analysis of how pore sizes and wall surface chemistry impact water flow capacity. Notably, the researchers identified slip boundaries arising from solid-liquid interactions, further revealing that these interactions introduce heterogeneous vis-

Yandy Scientific Press

*Corresponding author.
E-mail address: wwdong@upc.edu.cn (W. Wang); xieqiuheng1005@gmail.com (Q. Xie); hanwang@cup.edu.cn (H. Wang); suyuliang@upc.edu.cn (Y. Su); S.Rezaei-Gomari@tees.ac.uk (S. Rezaei-Gomari).

Received June 28, 2023; revised July 16, 2023; accepted July 29, 2023; available online August 3, 2023.

cosity within nanopores. Gravelle et al. (2013) investigated water flow through the hourglass shape of aquaporins with slip boundaries and discussed the interactions between slip boundaries and entrance effects. Zhang et al. (2017b) introduced an apparent permeability model to characterize the flow of shale oil by modifying the HP equation. Nonetheless, the intricate nature of the two-phase flow, involving slip velocity effects, it is difficult to characterize it by using theoretical equations except for some specific two-phase distributions, such as layered flow.

Furthermore, theoretical work considering slip effects on the two-phase layered flow has been carried out. Utilizing the modified slip boundary conditions, derived from the continuity-based HP equation, a novel relative permeability model specifically tailored to characterize gas-water two-phase flow in the nanoporous medium by Zhang et al. (2017a), however, their model was only suitable for the circular nanopore. Several works on oil-water flow under nano-confinement have been developed (Cui et al., 2019; Wang et al., 2022). According to the past model (Zhang et al., 2017a), Wang et al. (2019) developed a relative permeability model of oil-water flow with the slip boundary in the nanoporous medium, they found that the slip length is greatly related to the wettability. Subsequently, Zhan et al. (2020) employed molecular dynamics simulations (MDS) to modify Wang et al. (2019)'s model by considering liquid-liquid slip, a factor frequently disregarded in theoretical models.

Nonetheless, the aforementioned theoretical studies, which rely on a liquid layered distribution model within a single pore, face challenges in adequately addressing engineering application requirements. This challenge is particularly pronounced when dealing with intricate two-phase distributions occurring within porous media. Hence, the lattice Boltzmann method (LBM), as a direct simulation approach, finds extensive utilization for investigating liquid flow, particularly within intricate nanoporous media. The application of LBM is implemented by Zhang et al. (2022) to examine the interaction between capillary and viscous forces within a three-phase system. The forced imbibition process in natural rocks at four different injection rates is investigated via LBM (Liu et al., 2022). Zhao et al. (2018) employed the multiple-relaxation-time (MRT) LBM, utilizing slip length and effective viscosity data from MDS, to investigate the flow behaviors of water and alkanes within quartz nanoporous media. The study encompassed an analysis of contact angle mechanisms and end effects. Zhang et al. (2020) developed a novel LBM to investigate water flow in nanoporous structures in the shale which built a base to upscale the microporous structure. Zhao et al. (2021) adopted LBM to study the impact of nanopores geometry structure on confined water flow and established empirical formulas with different shapes based on the simulation structures. In the realm of two-phase flow, a variety of multicomponent-multiphase (MCMP) lattice Boltzmann models exist, among them being the color-gradient model (Gunstensen et al., 1991), Shan-Chen (pseudopotential) model (Shan and Chen, 1993; Shan and Doolen, 1995), and free energy model (Swift et al., 1996). Because of its simplicity and computational efficiency (Yang and Boek, 2013; Li and Luo, 2014; Zacharoudiou et al., 2018), the Shan-Chen pseudopotential model is very prevalent in the lattice Boltzmann (LB) community. Recently, Zhang et al. (2021) developed a pseudopotential-based LBM to investigate the gas-water two-phase flow in shale, however, their model is not suitable for two-phase flow with non-zero boundary slip velocity. Although LBM can precisely describe the fluid flow in the actual porous medium, its scale is still limited. Nevertheless, the combination of LBM and the pore network model (PNM) provides a novel way to upscale the problems of flow in the porous medium (Zhao et al., 2023). A novel PNM coupling the interphase drag and boundary slip was established to investigate the water-oil displacement process in low permeability porous media (Qin et al., 2023).

Accurate slip boundary conditions are crucial in nanoscale simulations to uphold the precision of LB simulation outcomes. Within the LB community, slip boundary conditions encompass bounce-back (BB), specular reflection (SR), and diffusive Maxwellian reflection (DM) (Wang et al., 2018). Nonetheless, these boundary conditions with the limitations of numerical errors, are not consistent with some analytical results hence over-predicting the slip velocity (Ansumali and Karlin, 2002; Lim et al., 2002; Nie et al., 2002; Verhaeghe et al., 2009). Addressing the aforementioned limitations, researchers introduced combined approaches for boundary conditions, including BB-SR (BSR) (Succi, 2002), DM-SR (DSR) (Tang et al., 2005; Szalmás, 2006), and DM-BB (DBB) (Guo et al., 2011; Yang et al., 2018) boundary conditions. To achieve non-zero slip velocity, the various slip conditions would be captured via selecting different combination parameters. While the mixed schemes of BSR and DSR are effective in introducing slip velocity along straight walls, their accuracy diminishes when simulating curved boundaries due to the non-local computation inherent to the SR component within these mixed approaches (Tao and Guo, 2015). This has been observed in the work performed by several researchers for the fluid flow with different slip boundaries in the LB community (Tao et al., 2017; Wang et al., 2021).

From the recent studies, the DBB boundary conditions are only used for single-phase flow, which is not suitable for MCMP slip flow in the nanoporous medium. This work presents the development of a novel multicomponent-multiphase multiple-relaxation-time lattice Boltzmann method (MCMP-MRT-LBM) coupled with a combined slip boundary condition, aimed at investigating two-phase slip flow behaviors. This innovative boundary condition results from the adjustment of conventional parameters in the diffusive Maxwellian reflection and half-way bounce-back scheme (HDBB), incorporating an enforced conservation requirement. Thereafter, the simulations for the layer, slug, and droplet types of two-phase flow in single pores, and two-phase flow in nanoporous media with complex wall geometries are adopted to verify the proposed model for simulating MCMP flow in the nanoporous medium with the non-zero slip velocity. To parameterize the effect of slip in single pores and nanoporous media, the slip length as a common way is adopted in this paper.

2. Multiple-relaxation-time LBM

In the LB community, the fluid flow in the porous medium is usually captured by the Bhatnagar-Gross-Krook (BGK) model (Zachariah et al., 2019; Gharibi and Ashrafizaadeh, 2020; Parvan et al., 2020). However, the poor numerical stability in the BGK model (d'Humières and Ginzburg, 2009), especially with slip boundary conditions (Wang et al., 2021), limits its applications. In this paper, the nanoscale MCMP pseudopotential model is developed to capture two-phase slip flow, and the MRT operator is adopted to maintain the stability of the model. The MRT LB equation can be presented as (Lallemand and Luo, 2000):

$$\begin{aligned} &f_{\sigma,\alpha}(\mathbf{x}+\mathbf{e}_\alpha\delta_t,t+\delta_t)-f_{\sigma,\alpha}(\mathbf{x},t)\\ &=-\mathbf{M}^{-1}\mathbf{\Lambda}\mathbf{M}(f_{\sigma,\alpha}(\mathbf{x},t)-f^{eq}_{\sigma,\alpha}(\mathbf{x},t))+\delta_t F'_\sigma \end{aligned} \tag{1}$$

where $f_{\sigma,\alpha}(\mathbf{x},t)$ is the distribution function of the component σ, δ_t is the time step, $\mathbf{e}_\alpha$ is the discrete velocity at α direction in the two-dimensional nine-velocity framework, $\mathbf{\Lambda}$ denotes the relaxation diagonal matrix, and F'_σ is the external force of the component σ. The transformation matrix $\mathbf{M}$ can be presented as:

$$\mathbf{M}=\begin{bmatrix} 1 & 1 & 1 & 1 & 1 & 1 & 1 & 1 & 1\\ -4 & -1 & -1 & -1 & -1 & 2 & 2 & 2 & 2\\ 4 & -2 & -2 & -2 & -2 & 1 & 1 & 1 & 1\\ 0 & 1 & 0 & -1 & 0 & 1 & -1 & -1 & 1\\ 0 & -2 & 0 & 2 & 0 & 1 & -1 & -1 & 1\\ 0 & 0 & 1 & 0 & -1 & 1 & 1 & -1 & -1\\ 0 & 0 & -2 & 0 & 2 & 1 & 1 & -1 & -1\\ 0 & 1 & -1 & 1 & -1 & 0 & 0 & 0 & 0\\ 0 & 0 & 0 & 0 & 0 & 1 & -1 & 1 & -1 \end{bmatrix} \tag{2}$$

The relaxation diagonal matrix $\mathbf{\Lambda}$ can be expressed as:

$$\mathbf{\Lambda}=\mathrm{diag}(s_0,s_1,s_2,s_3,s_4,s_5,s_6,s_7,s_8) \tag{3}$$

where $s_7=s_8=1/\tau$ depends on the kinematic viscosity, τ denotes the dimensional relaxation time, and the residual free parameters are defined as follows herein: $s_3=s_5=1$, and $s_1=s_2=s_4=s_6=1.1$. As a means of maintaining a continuous and smooth velocity profile across the interface, the relaxation parameters s_7 and s_8 across the interface are modified by Ba et al. (2016):

$$s_7=s_8=\begin{cases} 1/\tau_\sigma, & \rho^N>\zeta\\ \xi g_\sigma(\rho^N), & \zeta\geq\rho^N>0\\ \xi g_{\sigma'}(\rho^N), & 0\geq\rho^N\geq-\zeta'\\ 1/\tau_{\sigma'}, & \rho^N<-\zeta \end{cases} \tag{4}$$

where τ_σ and $\tau_{\sigma'}$ are the relaxation times of component σ and σ' respectively, ξ controls liquid-liquid velocity continuity, ζ is an adjustable parameter related to the interface thickness and equals 0.8 in this paper. $\rho^N=(\rho_\sigma-\rho_{\sigma'})/(\rho_\sigma+\rho_{\sigma'})$ is the phase-field equation characterizing the interfacial region, and for the pseudopotential model, the thickness of the interfacial area is roughly 6-10 lattice units (lu) (Yang and Boek, 2013). For the oil and water phase, there is a certain physical interface thickness of about 0.7 nm (Wang et al., 2019). g_σ and $g_{\sigma'}$ are parabolic functions given by Reis and Phillips (2007).

By considering the transformation matrix $\mathbf{M}$, Eq. (1) is revised in the form of the moments:

$$\mathbf{m}^*_{\sigma,\alpha}=\mathbf{m}_{\sigma,\alpha}-\mathbf{\Lambda}\left(\mathbf{m}_{\sigma,\alpha}-\mathbf{m}^{eq}_{\sigma,\alpha}\right)+\delta_t\left(\mathbf{I}-\frac{\mathbf{\Lambda}}{2}\right)\mathbf{S}_\sigma \tag{5}$$

where $\mathbf{m}_{\sigma,\alpha}=\mathbf{M}f_{\sigma,\alpha}$, $\mathbf{m}^{eq}_{\sigma,\alpha}=\mathbf{M}f^{eq}_{\sigma,\alpha}$ are the moments and the equilibria of moments, $f_{\sigma,\alpha}(\mathbf{x}+\mathbf{e}_\alpha\delta_t,t+\delta_t)=f^*_{\sigma,\alpha}(\mathbf{x},t)$ is the streaming process, $f^*_{\sigma,\alpha}$ denotes the post-collision equation, and $f^*_{\sigma,\alpha}=\mathbf{M}^{-1}\mathbf{m}^*_{\sigma,\alpha}$. $\mathbf{I}$ represents the unit tensor.

The forcing term at the moment space is defined by Li et al. (2013):

$$\mathbf{S}_\sigma=\begin{bmatrix} 0\\ 6\left(u^{eq}_x F_{\sigma,x}+u^{eq}_y F_{\sigma,y}\right)\\ -6\left(u^{eq}_x F_{\sigma,x}+u^{eq}_y F_{\sigma,y}\right)\\ F_{\sigma,x}\\ -F_{\sigma,x}\\ F_{\sigma,y}\\ -F_{\sigma,y}\\ 2\left(u^{eq}_x F_{\sigma,x}-u^{eq}_y F_{\sigma,y}\right)\\ \left(u^{eq}_x F_{\sigma,y}+u^{eq}_y F_{\sigma,x}\right) \end{bmatrix} \tag{6}$$

where $\mathbf{F}_\sigma=(F_{\sigma,x},F_{\sigma,y})$ is the external total force, and $\mathbf{F}_\sigma=\mathbf{F}_{\sigma,\mathrm{int}}+\mathbf{F}_{\sigma,\mathrm{ads}}+\mathbf{F}_{\sigma,\mathrm{b}}$. $\mathbf{F}_{\sigma,\mathrm{int}}$ denotes the interaction force between two different components, $\mathbf{F}_{\sigma,\mathrm{ads}}$ represents the adhesion force between each component and the solid, and $\mathbf{F}_{\sigma,\mathrm{b}}$ is the force imposing on the body of each component. For MCMP flow, each force term can be presented as:

$$\mathbf{F}_{\sigma,\mathrm{int}}(\mathbf{x},t)=-G_{\sigma\sigma'}\psi_\sigma(\mathbf{x},t)\sum_\alpha w\left(|\mathbf{e}_\alpha|^2\right)\psi_{\sigma'}(\mathbf{x}+\mathbf{e}_\alpha\delta_t)\mathbf{e}_\alpha \tag{7}$$

$$\mathbf{F}_{\sigma,\mathrm{ads}}(\mathbf{x},t)=-G_{\sigma s}\psi_\sigma(\mathbf{x},t)\sum_\alpha w\left(|\mathbf{e}_\alpha|^2\right)s(\mathbf{x}+\mathbf{e}_\alpha\delta_t)\mathbf{e}_\alpha \tag{8}$$

$$\mathbf{F}_{\sigma,\mathrm{b}}=\left(F_{\sigma,b,x},F_{\sigma,b,y}\right) \tag{9}$$

where $G_{\sigma\sigma'}$ represents the strength of the interaction between different components, σ' represent the other phase compared to σ, $G_{\sigma s}$ denotes the strength of the interaction between each component and the solid. $\psi_\sigma=1-\exp(-\rho_\sigma)$ expresses the pseudopotential in the pseudopotential model, and $\rho_\sigma=\sum_\alpha f_{\sigma,\alpha}$ is macroscopic density. $s(\mathbf{x}+\mathbf{e}_\alpha\delta_t)$ is a switch function to classify the different phase nodes, it equals zero for the liquid node and unity for the solid node. $w\left(|\mathbf{e}_\alpha|^2\right)$ denotes the weight coefficient at α direction for calculating each force term:

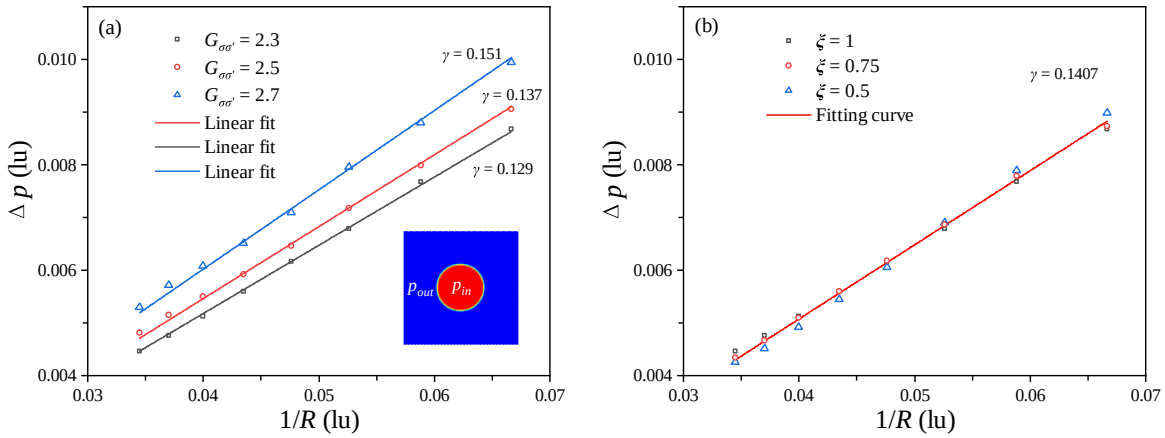

Fig. 1. (a) The relationship between Δp and $1/R$ and (b) the effect of ξ on the surface tension.

$$w\left(|\mathbf{e}_\alpha|^2\right)=\begin{cases}\dfrac{1}{3}, |\mathbf{e}_\alpha|^2=1\\ \dfrac{1}{12}, |\mathbf{e}_\alpha|^2=2\end{cases} \tag{10}$$

The equilibria of moments $\mathbf{m}_\sigma^{eq}$ is given by (Lallemand and Luo, 2000; Yang et al., 2020):

$$\mathbf{m}_\sigma^{eq}=\rho_\sigma\left[1,-2+3\left(u_x^{eq^2}+u_y^{eq^2}\right),1-3\left(u_x^{eq^2}+u_y^{eq^2}\right),u_x^{eq},-u_x^{eq},u_y^{eq},-u_y^{eq},u_x^{eq^2}-u_y^{eq^2},u_x^{eq}u_y^{eq}\right]^T \tag{11}$$

In MCMP-MRT-LBM, the equilibrium velocity is calculated as:

$$\mathbf{u}^{eq}=\left(u_x^{eq},u_y^{eq}\right)=\frac{\sum_\sigma \rho_\sigma \mathbf{u}_\sigma}{\sum_\sigma \rho_\sigma} \tag{12}$$

The velocity $\mathbf{u}_\sigma$ of the component σ can be expressed by:

$$\rho_\sigma \mathbf{u}_\sigma=\sum_\alpha \mathbf{e}_\alpha f_{\sigma,\alpha}+0.5\delta_t \mathbf{F}_\sigma \tag{13}$$

The HDBB boundary for the slip flow is adopted to obtain the unknown distribution functions, which is solved:

$$f_{\sigma,\alpha}=(1-r_\sigma)\,\bar{f}_{\sigma,\bar{\alpha}}+r_\sigma f_{\sigma,\alpha}^{eq}(\mathbf{u}_{wall}) \tag{14}$$

where $\bar{f}_{\sigma,\bar{\alpha}}$ denotes the post-collision distribution function in reverse directions. $\mathbf{u}_{wall}$ represents the velocity of the solid wall and equals zero herein, r_σ characterizes the degree of the slip of the component σ.

The equilibrium distribution function for each component $f_{\sigma,\alpha}^{eq}$ is expressed as:

$$f_{\sigma,\alpha}^{eq}(\rho_\sigma,\mathbf{u}^{eq})=w_\alpha\rho_\sigma\left[1+\frac{\mathbf{e}_\alpha\cdot\mathbf{u}^{eq}}{c_s^2}+\frac{(\mathbf{e}_\alpha\cdot\mathbf{u}^{eq})^2}{2c_s^4}-\frac{\mathbf{u}^{eq^2}}{2c_s^2}\right] \tag{15}$$

where w_α denotes the weight and can be expressed as: $w_0=4/9$, $w_{1-4}=1/9$, $w_{5-8}=1/36$.

In our previous work (Wang et al., 2021), this combination boundary condition was adopted to investigate single-phase flow in the nanoporous medium. Compared with single-phase flow, capturing MCMP slip flow by utilizing the HDBB boundary does not satisfy mass conservation. To avoid this problem, the conventional combination parameter r_σ is modified by adding a forced conservation condition $c_\sigma=\left[\sum_\alpha s(\mathbf{x}+\mathbf{e}_\alpha\delta_t)\bar{f}_{\sigma,\bar{\alpha}}\right]/\left[\sum_\alpha s(\mathbf{x}+\mathbf{e}_\alpha\delta_t)f_{\sigma,\alpha}^{eq}(\mathbf{u}_{wall})\right]$:

$$f_{\sigma,\alpha}=(1-r_\sigma)\,\bar{f}_{\sigma,\bar{\alpha}}+r_\sigma c_\sigma f_{\sigma,\alpha}^{eq}(\mathbf{u}_{wall}) \tag{16}$$

Due to the nature of the pseudopotential model, a small amount of component σ' would exist in component σ. The slip boundary conditions of the component σ' in component σ can be expressed according to the equation for component σ:

$$f_{\sigma',\alpha}=(1-r_\sigma)\,\bar{f}_{\sigma',\bar{\alpha}}+r_\sigma c_{\sigma'} f_{\sigma',\alpha}^{eq}(\mathbf{u}_{wall}) \tag{17}$$

3. Model verification

Laplace's law and contact angle test are used to verify that the two-phase pseudopotential model herein is correct. The innovation of the proposed model is two-phase slip flow on the solid wall. Therefore, the proposed model should also demonstrate that it can achieve different two-phase boundary slip velocities, which is emphasized in Section. 4.

3.1 Laplace's law

Satisfying Laplace's law is a common way to verify MCMP-MRT-LBM. Initially, a static liquid droplet with various radii is initialized in the middle of the domain with 100×100 lattices. The surface tension (γ) between two phases is up to the pressure difference ($p_{in}-p_{out}$) and the droplet radius (R):

$$\Delta p=p_{in}-p_{out}=\frac{\gamma}{R} \tag{18}$$

For the MCMP system, the pressure of the liquid can be defined by:

$$p=c_s^2\left(\rho_\sigma+\rho_{\sigma'}\right)+c_s^2 G_{\sigma\sigma'}\psi_\sigma\psi_{\sigma'} \tag{19}$$

Fig. 1(a) illustrates the relationship between Δp and $1/R$,

which means that the simulated outcomes are consistent with the theory. The slopes of the fitting lines represent the surface tension in lu. With an increase in liquid-liquid interaction force, the lattice surface tension increases. In addition, the $G_{\sigma\sigma'} = 2.5$ is used in the following simulations and discussions. In Eq. (4), an adjustable parameter ξ is applied, and it has small effects on the surface tension as depicted in Fig. 1(b). Therefore, in this work, it is deemed that the surface tension is independent of the parameter ξ.

3.2 Contact angle test

The solid density is set to 0.5, and adjusting $G_{\sigma s}$ can achieve different contact angles. First, one phase shaped in a rectangular geometry is placed on a solid wall in a two-dimensional domain. Due to solid-liquid and liquid-liquid interactions, the liquid gradually transforms into a droplet on the solid, and the contact angle is solved by the profile of the droplet (Schmieschek and Harting, 2011). The different contact angles could be achieved by changing $G_{\sigma s}$ as depicted in Fig. 2. Additionally, with different slip boundary conditions, the corresponding relationships between $G_{\sigma s}$ and contact angles are different. Therefore, when the different slip lengths are applied in the simulations, the appropriate contact angle needs to be properly re-selected.

4. Results and discussion

When the two-phase liquid flows in a single pore, the flow patterns include layered flow, slug flow, and droplet flow. Also, the two-phase flow with random phase distributions in oil reservoirs is very prevalent. In this part, the two-phase flow in a single pore with different phase distributions and slip boundary conditions is elaborately simulated and discussed. In this simulation, a series of the constant external body force ($F_{b,x} = 1 \times 10^{-5}$, $F_{b,x} = 5 \times 10^{-5}$, and $F_{b,x} = 1 \times 10^{-3}$) along the x direction is used. The HDBB boundary with different combination parameters is used for the solid wall, and the periodic condition is adopted at both the left and right boundaries.

4.1 Layered two-phase slip flow

First, the classical two-phase layered slip flow behaviors are discussed. As represented in Fig. 3, the two-phase layered flow models are developed.

For the first case, the theoretical equation is utilized to verify the rationality of the proposed model, and the velocity equations of the interfacial and bulk liquid are shown as follows:

$$u(y) = \begin{cases} \dfrac{y(H-y)F_{b,x}}{2\mu_\sigma} + C_1, & 0 \le y \le \delta \text{ and } H-\delta \le y \le H \\ \dfrac{y(H-y)F_{b,x}}{2\mu_{\sigma'}} + C_2, & \delta \le y \le H-\delta \end{cases} \tag{20}$$

where $u(y)$ is the velocity along y axis, y is the location along y axis, H is the height of pore, μ is the viscosity of each component, C_1 and C_2 are the parameters depending on the slip length l_s.

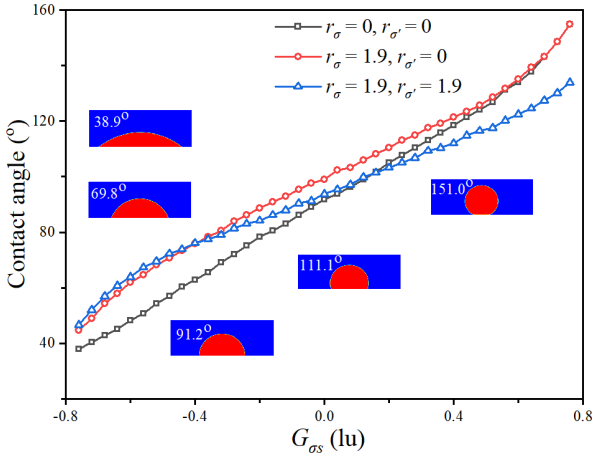

Fig. 2. The relationship between the contact angle and $G_{\sigma s}$ with different combination parameters.

The continuity of the velocity between the two phases can be guaranteed based on the boundary conditions as indicated in Fig. 3(c), which are expressed as (Wang et al., 2019):

$$l_s \frac{\partial u_\sigma}{\partial y}\Big|_{y=0} = u_\sigma|_{y=0} \tag{21}$$

$$u_\sigma|_{y=\delta} = u_{\sigma'}|_{y=\delta} \tag{22}$$

According to Eqs. (21) and (22), the parameters C_1 and C_2 can be obtained, and the velocities of phase σ and σ' can be defined as:

$$\frac{u(y)}{F_{b,x}} = \begin{cases} \dfrac{y(H-y)}{2\mu_\sigma} + \dfrac{l_s H}{2\mu_\sigma}, & 0 \le y \le \delta \text{ and } H-\delta \le y \le H \\ \dfrac{y(H-y)}{2\mu_{\sigma'}} + \dfrac{1}{2\mu_\sigma}\left(H\delta - \delta^2\right) - \dfrac{1}{2\mu_{\sigma'}}\left(H\delta - \delta^2\right) & \\ \quad + \dfrac{l_s H}{2\mu_\sigma}, & \delta \le y \le H-\delta \end{cases} \tag{23}$$

In the simulations, the thickness of the interfacial region is around 6 lu. Based on Eq. (4), a continuous and smooth velocity profile across the interfacial region can be maintained. Fig. 4 shows the smooth velocity profiles with different slip boundary conditions and viscosity ratios. From velocity profiles with zero slip velocity ($r = 0$) in Figs. 4(a) and 4(b), the results calculated by analytical equations fit well with that obtained by LBM. With a combination parameter r equaling 1.9, the non-zero slip velocity is simulated, as depicted in Figs. 4(c) and 4(d). Based on the analytical equations, the slip length l_s is modified to fit the simulated velocities. With the slip length l_s equaling 50.5 and 25.6 in Figs. 4(c) and 4(d), the velocities calculated by analytical equations are in agreement with that obtained by LBM. For the two-phase layered flow model in Fig. 3(b), the velocity distributions with different slip lengths are given in Fig. 5. From Fig. 5(a), with an increasing combination parameter of the phase σ', the slip velocity on the solid wall increases. Additionally, the slip velocity of phase σ can also be affected by the increasing combination parameter of the phase σ'. Fig. 5(b) shows similar results. It means that the proposed model can readily capture the multiphase flow with the different slip conditions for each phase.

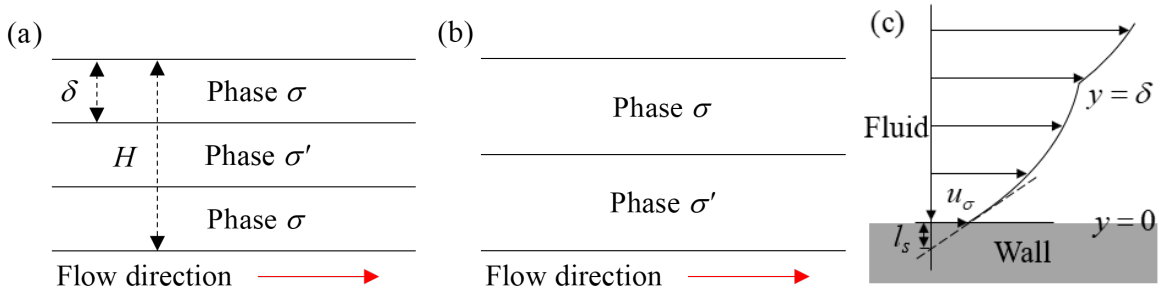

Fig. 3. Two-phase layered flow models for different phase distributions for (a) and (b), and schematic of the slip velocity (c), which is revised from Berg et al. (2008)'s work.

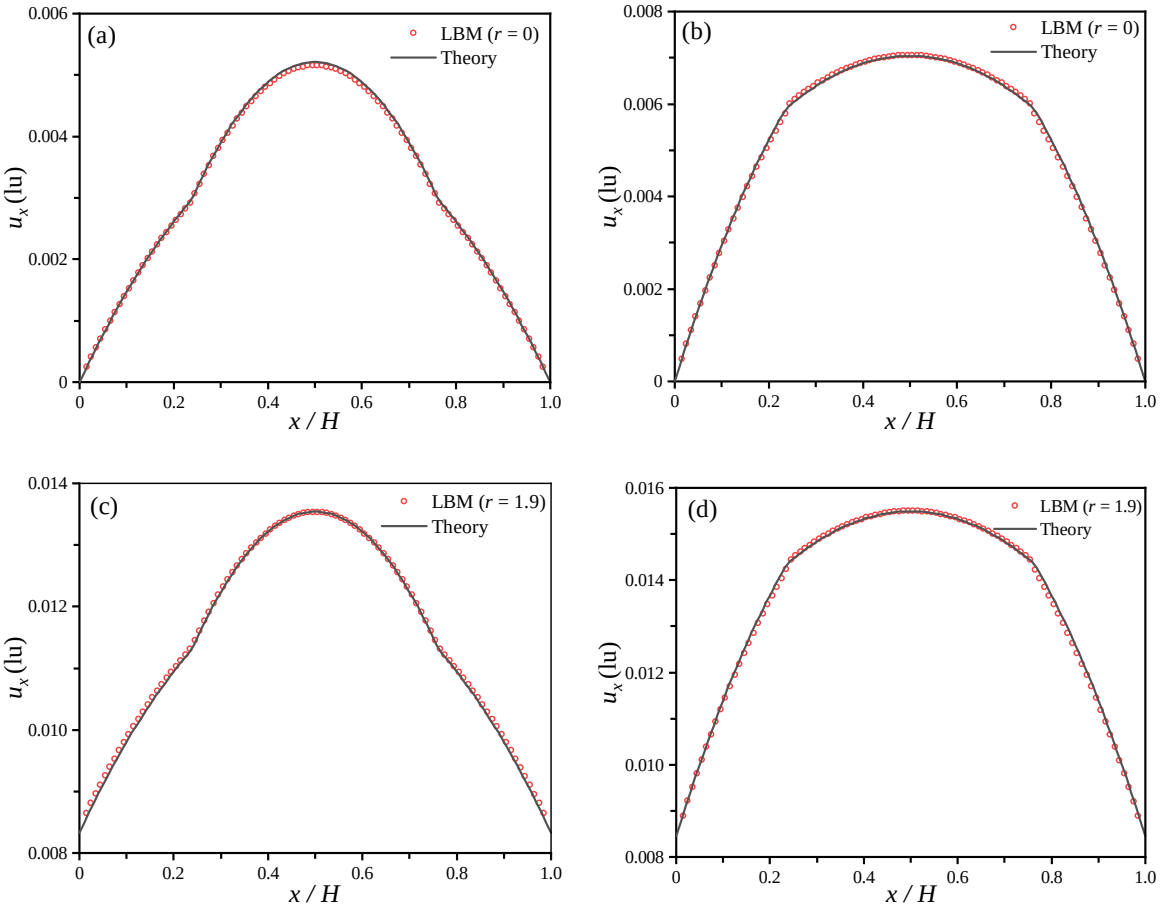

Fig. 4. Velocities with different slip boundary conditions and viscosity ratios of layered flow model 'A'. In (a) and (c), $\mu_\sigma/\mu_{\sigma'} = 0.5$, in (b) and (d), $\mu_\sigma/\mu_{\sigma'} = 2$.

4.2 Characterization of the slip length

As shown in Section 4.1, with combination parameter r equaling 1.9, we can determine the slip length l_s equaling 50.5 with $\mu_\sigma/\mu_{\sigma'} = 0.5$ by analytical fitting. Therefore, the dependence of the slip length l_s on the combination parameter r can be quantitatively characterized. With a constant combination parameter, the velocity of the two-phase flow can be obtained. The slip length can be fitted through the analytical Eq. (23). Under the layered flow model in Fig. 3(a), the relationships among the combination parameter, the slip length, and $G_{\sigma s}$ are acquired as depicted in Fig. 6. The calculated slip length increases with the increment of the combination parameter. With the decrease of the water wettability, the slip length gradually increases from $l_s = 0.41/(1+\cos\theta)^2$ (Wu et al., 2017). The same results are obtained from our simulations with an increasing solid-liquid interaction parameter $G_{\sigma s}$ (Fig. 6) where the contact angle of phase σ increases which indicates the decrease of the phase σ wettability, consequently the slip length increases. It confirms that the wettability effects on the

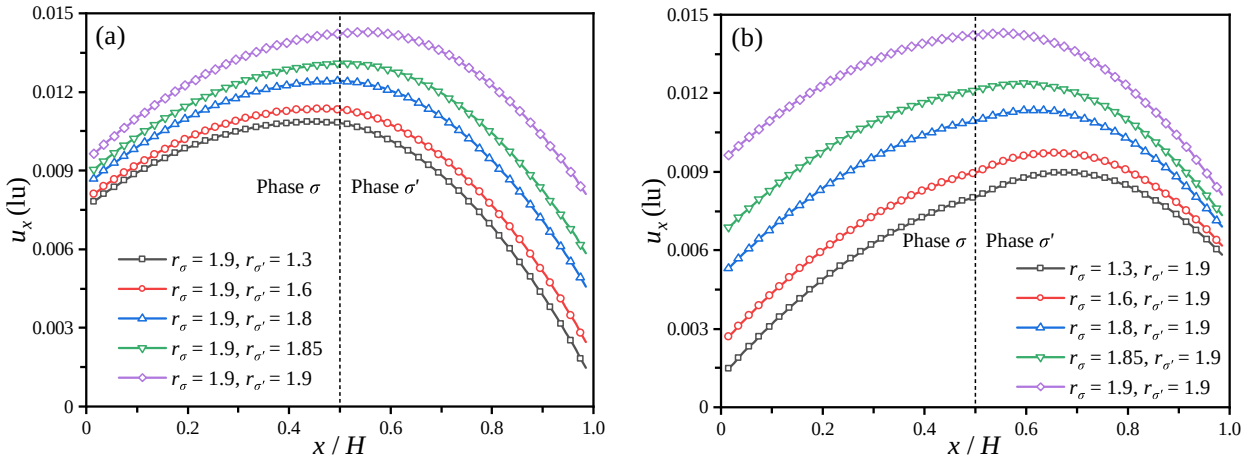

Fig. 5. Velocities with different slip boundary conditions of a layered flow model 'B'. (a) Different slip boundary conditions of phase σ', (b) different slip boundary conditions of phase σ.

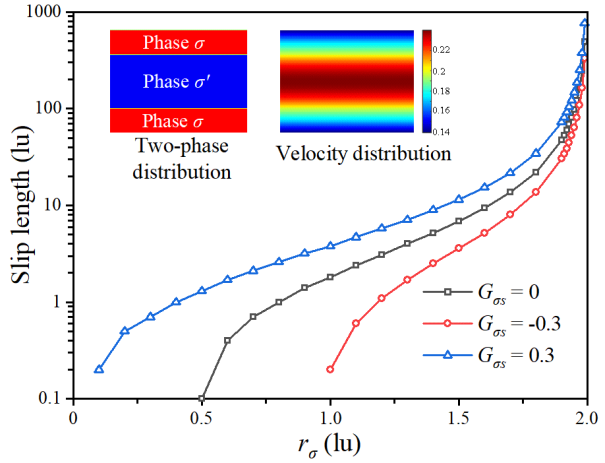

Fig. 6. Combination parameters versus the slip length under different solid-liquid interaction parameters.

slip velocity can be investigated by our model, the relationship between $G_{\sigma s}$ and the wettability is indicated in Fig. 2.

4.3 Two-phase slip slug flow

The slug flow behaviors under different slip boundary conditions are analyzed in this section. The static two-phase distribution is shown in Fig. 7(a) for a constant contact angle of phase σ and phase σ'. Exerting a constant external body force $F_{b,x} = 5 \times 10^{-5}$, the dynamics phase distribution is shown in Fig. 7(b).

The velocity profiles of phase σ and phase σ' are captured under four slip boundary conditions as shown in Fig. 8. When the combination parameters equal zero, the boundary velocity is zero. Initiating the combination parameters of two phases equaling 1.9 and 1.9, or 1.9 and 0, velocity profiles are parabolic with a non-zero slip velocity. The slip boundary results in a decreasing hydrodynamic resistance of liquid flow through the pore, which means that the velocity significantly increases.

4.4 Liquid droplet flow on the solid wall and two-phase flow in porous media

The flow of droplets across pore walls is simulated in this section, and the phase distributions of droplets with different combination parameters are given in Fig. 9.

The flow capacity of the droplet increases when the slip boundary conditions are implemented. The random phase distribution of two phases in porous media with slip boundary conditions is also investigated. The two phases are randomly initialized in the porous medium and separated gradually due to the interfacial force between different phases. By exerting a constant external body force $F_{b,x} = 1 \times 10^{-3}$ and the slip boundary conditions ($r_\sigma = 1.9, r_{\sigma'} = 1.9$), the two-phase slip flow on the complex wall geometry is implemented. The two-phase distributions versus time are shown in Fig. 10.

To explore the effects of slip boundary on relative permeability and flow capacity, first, different slip boundary conditions of component σ ($r_\sigma = 0, r_\sigma = 1.5, r_\sigma = 1.9$) and a constant slip boundary condition of the component σ' ($r_{\sigma'} = 1.9$) are selected. The slip length increases with the increment of r_σ. The volume flux Q_σ of component σ under different boundary conditions is calculated by Eq. (24). With the increment of slip length, the volume flux gradually grows as depicted in Fig. 11(a) indicating the gradual growth of flow capacity of component σ. The relative permeability can be calculated by Eqs. (25) and (26). From Fig. 11(b), the results demonstrate that the slip boundary condition has irregular effects on the relative permeability of component σ based on the selected porous media:

$$Q_\sigma(S_\sigma) = \frac{\int_{|y|=0}^{t_\sigma} u_\sigma dy}{N_x} \tag{24}$$

$$k_{r\sigma}(S_\sigma) = \frac{\int_{|y|=0}^{t_\sigma} u_\sigma dy}{\int_{|y|=0}^{t} u_\sigma dy} \tag{25}$$

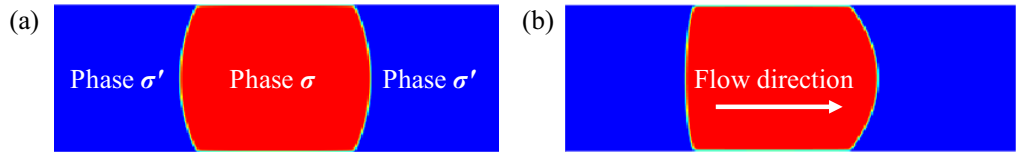

Fig. 7. Schematic of the two-phase slug flow. (a) Static phase distribution, (b) dynamic phase distribution, and $\mu_\sigma/\mu_{\sigma'} = 2$.

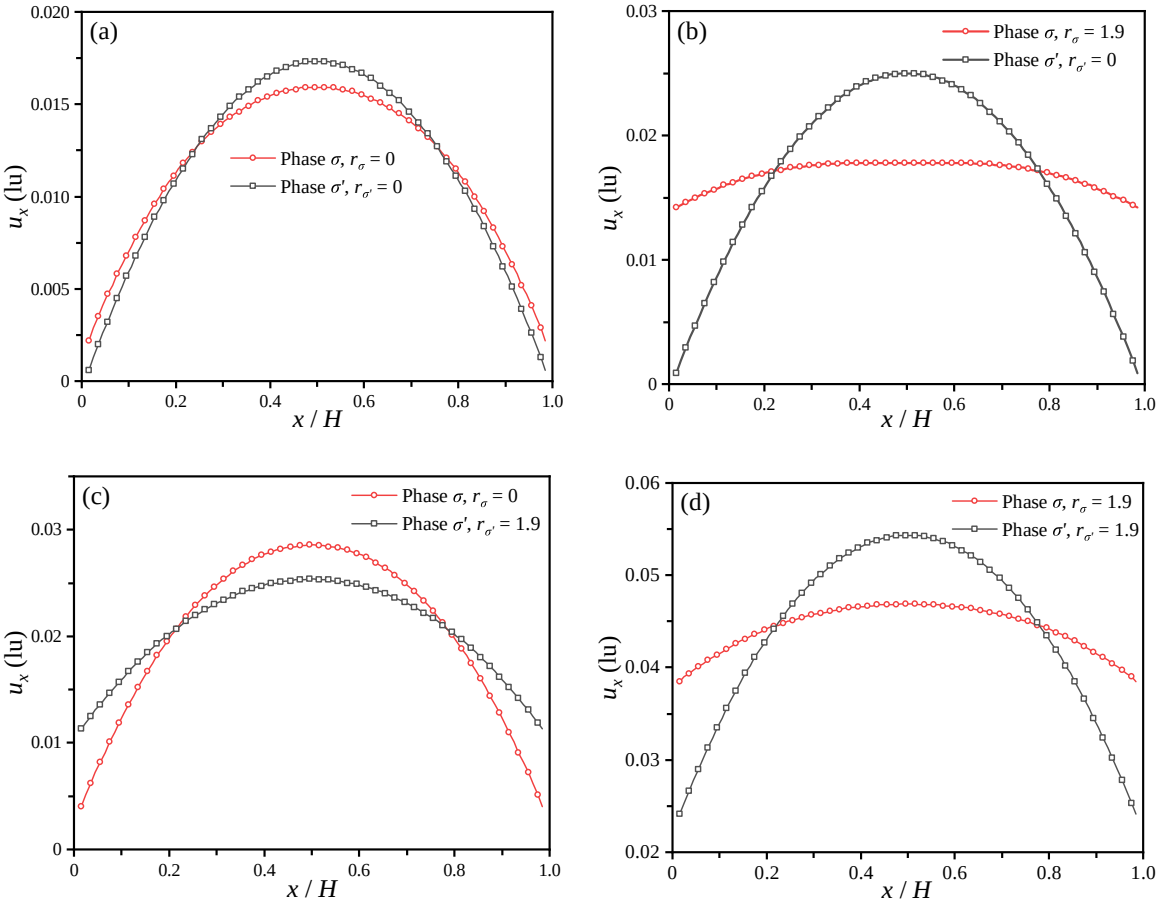

Fig. 8. Velocity profiles with different slip boundary conditions. $r_\sigma = 0, r_{\sigma'} = 0$ for (a), $r_\sigma = 1.9, r_{\sigma'} = 0$ for (b), $r_\sigma = 0, r_{\sigma'} = 1.9$ for (c) and $r_\sigma = 1.9, r_{\sigma'} = 1.9$ for (d).

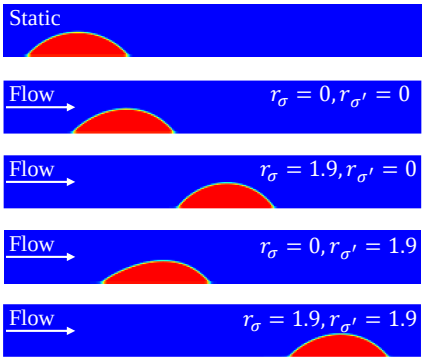

Fig. 9. The phase distribution of liquid droplet flow on the pore wall with different boundary conditions in the same simulated period, where the red denotes the component σ, and the blue represents the component σ'.

$$k_{r\sigma'}(S_\sigma) = \frac{\int_{|y|=0}^{t_{\sigma'}} u_{\sigma'} dy}{\int_{|y|=0}^{t} u_{\sigma'} dy} \tag{26}$$

where $k_{r\sigma}$ and $k_{r\sigma'}$ are the relative permeability, t is the total lattice, u_σ and $u_{\sigma'}$ are the velocity in each lattice, N_x is lattice number in x direction. The proposed model can simulate two-phase slip flow with different boundary slip lengths in porous media. Compared with the theory or MDS, this kind of pore-scale model can handle the slip effect not only in a single pore but also in nanoporous media which is more general in most applications.

5. Conclusions

A novel mesoscopic LBM for two-phase flow in nanoscale space considering the boundary conditions of non-zero slip

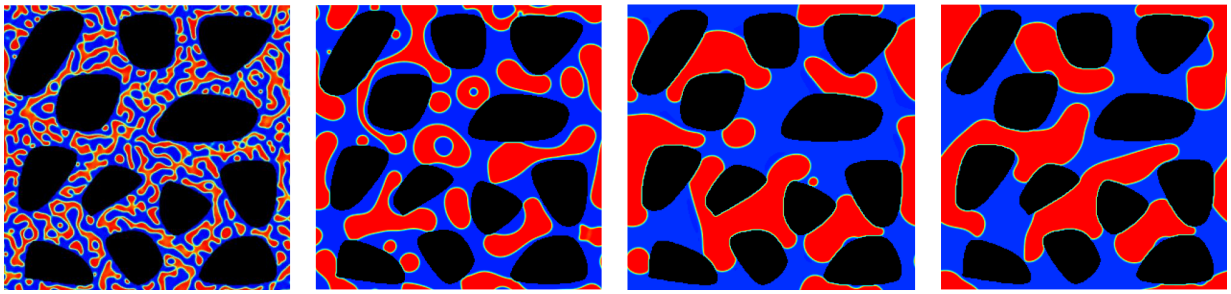

Fig. 10. The phase distribution of liquids with the slip boundary condition ($r_\sigma = 1.9, r_{\sigma'} = 1.9$). The black represents the solid. lt is the lattice time. The computational domain is $N_x = 300$ for length and $N_y = 300$ for width.

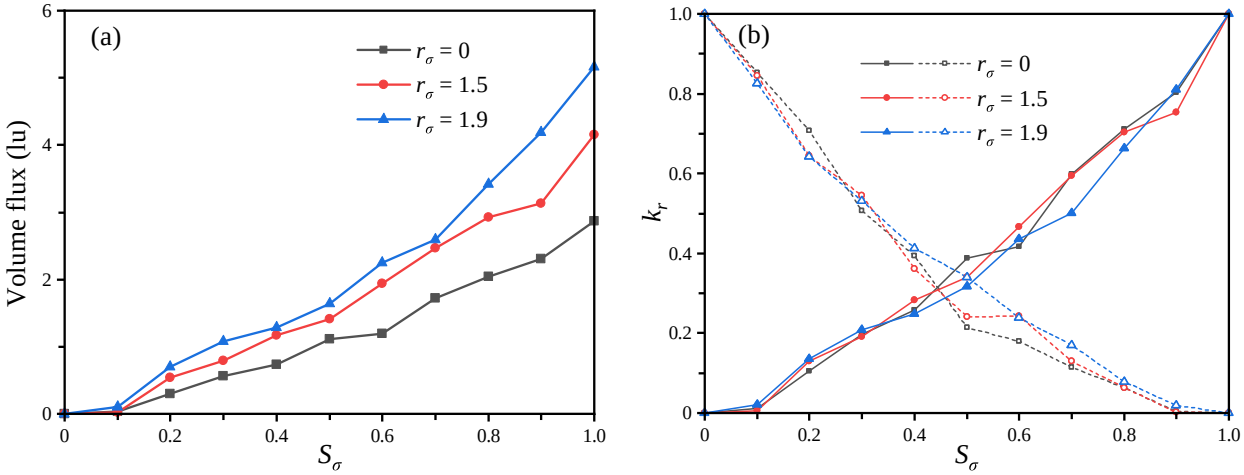

Fig. 11. (a) Volume flux and (b) relative permeability with changes in the saturation under different slip boundary conditions.

velocity is developed. This is done by modifying the conventional combination parameter of the HDBB boundary considering a forced conservation condition. It can capture the slip effect in both nanopores and nanoporous media to give an in-depth understanding of multiphase flow in shale oil reservoirs and other applications in the nanospace.

According to the analysis of the two-phase flow simulations for the layer, slug, and droplet types in single pores, and two-phase flow in the porous medium with complex geometry, it is observed that the proposed schemes of two-phase slip boundary conditions are particularly suitable for MCMP flow with a non-zero slip velocity. The slip effects on volume flux and relative permeability are also elaborated, and the results indicate that the slip boundary can promote the liquid flow capacity. However, the slip effects on relative permeability are irregular and up to selected porous media. While promising results are obtained, the novel model could be applied to simulate oil, gas, and water flow in nanoscale space and calculate the relative permeability.

Acknowledgements

This study was supported by the National Natural Science Foundation of China (Nos. 52274056, U22B2075 and 51974348).

Conflict of interest

The authors declare no competing interest.

References

Ansumali, S., Karlin, I. V. Kinetic boundary conditions in the lattice Boltzmann method. Physical Review E, 2002, 66(2): 026311.

Ba, Y., Liu, H., Li, Q., et al. Multiple-relaxation-time color-gradient lattice Boltzmann model for simulating two-phase flows with high density ratio. Physical Review E, 2016, 94(2): 023310.

Berg, S., Cense, A. W., Hofman, J. P., et al. Two-phase flow in porous media with slip boundary condition. Transport in Porous Media, 2008, 74: 275-292.

Cui, R., Feng, Q., Chen, H., et al. Multiscale random pore network modeling of oil-water two-phase slip flow in shale matrix. Journal of Petroleum Science and Engineering, 2019, 175: 46-59.

Cui, Y., Wei, Q., Park, H., et al. Nanowire nanosensors for highly sensitive and selective detection of biological and

chemical species. Science, 2001, 293(5533): 1289-1292.
Das, R., Ali, M. E., Hamid, S. B. A., et al. Carbon nanotube membranes for water purification: a bright future in water desalination. Desalination, 2014, 336: 97-109.
d'Humières, D., Ginzburg, I. Viscosity independent numerical errors for Lattice Boltzmann models: From recurrence equations to "magic" collision numbers. Computers & Mathematics with Applications, 2009, 58(5): 823-840.
Feng, Q., Xu, S., Xing, X., et al. Advances and challenges in shale oil development: A critical review. Advances in Geo-Energy Research, 2020, 4(4): 406-418.
Geng, J., Kim, K., Zhang, J., et al. Stochastic transport through carbon nanotubes in lipid bilayers and live cell membranes. Nature, 2014, 514(7524): 612-615.
Gharibi, F., Ashrafizaadeh, M. Darcy and inertial fluid flow simulations in porous media using the non-orthogonal central moments lattice Boltzmann method. Journal of Petroleum Science and Engineering, 2020, 194: 107572.
Gravelle, S., Joly, L., Detcheverry, F., et al. Optimizing water permeability through the hourglass shape of aquaporins. Proceedings of the National Academy of Sciences, 2013, 110(41): 16367-16372.
Gunstensen, A. K., Rothman, D. H., Zaleski, S., et al. Lattice Boltzmann model of immiscible fluids. Physical Review A, 1991, 43(8): 4320-4327.
Guo, Z., Shi, B., Zheng, C. Velocity inversion of micro cylindrical Couette flow: A lattice Boltzmann study. Computers & Mathematics with Applications, 2011, 61(12): 3519-3527.
Ham, S., Narayanan Nair, A. K., Sun, S., et al. Modulation of slippage at brine-oil interfaces by surfactants: The effects of surfactant density and tail length. Physics of Fluids, 2022, 34(2): 022106.
Lallemand, P., Luo, L. S. Theory of the lattice Boltzmann method: Dispersion, dissipation, isotropy, Galilean invariance, and stability. Physical Review E, 2000, 61(6): 6546-6562.
Li, Q., Luo, K. Thermodynamic consistency of the pseudopotential lattice Boltzmann model for simulating liquid-vapor flows. Applied Thermal Engineering, 2014, 72(1): 56-61.
Li, Q., Luo, K., Li, X. Lattice Boltzmann modeling of multiphase flows at large density ratio with an improved pseudopotential model. Physical Review E, 2013, 87(5): 053301.
Lim, C. Y., Shu, C., Niu, X. D., et al. Application of lattice Boltzmann method to simulate microchannel flows. Physics of Fluids, 2002, 14(7): 2299-2308.
Liu, Y., Berg, S., Ju, Y., et al. Systematic investigation of corner flow impact in forced imbibition. Water Resources Research, 2022, 58(10): e2022WR032402.
Mattia, D., Calabrò, F. Explaining high flow rate of water in carbon nanotubes via solid-liquid molecular interactions. Microfluidics and Nanofluidics, 2012, 13(1): 125-130.
Nie, X., Doolen, G. D., Chen, S. Lattice-Boltzmann simulations of fluid flows in MEMS. Journal of Statistical Physics, 2002, 107: 279-289.
Parvan, A., Jafari, S., Rahnama, M., et al. Insight into particle retention and clogging in porous media; a pore scale study using lattice Boltzmann method. Advances in Water Resources, 2020, 138: 103530.
Reis, T., Phillips, T. N. Lattice Boltzmann model for simulating immiscible two-phase flows. Journal of Physics A: Mathematical and Theoretical, 2007, 40(14): 4033-4053.
Qin, X., Xia, Y., Qiao, J., et al. Modeling of multiphase flow in low permeability porous media: Effect of wettability and pore structure properties. Journal of Rock Mechanics and Geotechnical Engineering, 2023, in press, https://doi.org/10.1016/j.jrmge.2023.06.007.
Schmieschek, S., Harting, J. Contact angle determination in multicomponent lattice Boltzmann simulations. Communications in Computational Physics, 2011, 9(5): 1165-1178.
Seyyedattar, M., Zendehboudi, S., Butt, S. Molecular dynamics simulations in reservoir analysis of offshore petroleum reserves: A systematic review of theory and applications. Earth-Science Reviews, 2019, 192: 194-213.
Shan, X., Chen, H. Lattice Boltzmann model for simulating flows with multiple phases and components. Physical Review E, 1993, 47(3): 1815-1819.
Shan, X., Doolen, G. Multicomponent lattice-Boltzmann model with interparticle interaction. Journal of Statistical Physics, 1995, 81(1-2): 379-393.
Shin, S., Kim, A. R., Um, S. Computational prediction of nanoscale transport characteristics and catalyst utilization in fuel cell catalyst layers by the lattice Boltzmann method. Electrochimica Acta, 2018, 275: 87-99.
Succi, S. Mesoscopic modeling of slip motion at fluid-solid interfaces with heterogeneous catalysis. Physical Review Letters, 2002, 89(6): 064502.
Swift, M. R., Orlandini, E., Osborn, W. R., et al. Lattice Boltzmann simulations of liquid-gas and binary fluid systems. Physical Review E, 1996, 54(5): 5041-5052.
Szalmás, L. Slip-flow boundary condition for straight walls in the lattice Boltzmann model. Physical Review E, 2006, 73(6): 066710.
Tang, G., Tao, W., He, Y. Lattice Boltzmann method for gaseous microflows using kinetic theory boundary conditions. Physics of Fluids, 2005, 17(5): 058101.
Tao, S., Guo, Z. Boundary condition for lattice Boltzmann modeling of microscale gas flows with curved walls in the slip regime. Physical Review E, 2015, 91(4): 043305.
Tao, S., Zhang, H., Guo, Z. Drag correlation for micro spherical particles at finite Reynolds and Knudsen numbers by lattice Boltzmann simulations. Journal of Aerosol Science, 2017, 103: 105-116.
Verhaeghe, F., Luo, L. S., Blanpain, B. Lattice Boltzmann modeling of microchannel flow in slip flow regime. Journal of Computational Physics, 2009, 228(1): 147-157.
Wang, X., Li, J., Jiang, W., et al. Characteristics, current exploration practices, and prospects of continental shale oil in China. Advances in Geo-Energy Research, 2022, 6(6): 454-459.
Wang, H., Su, Y., Wang, W., et al. Relative permeability model of oil-water flow in nanoporous media considering

multi-mechanisms. Journal of Petroleum Science and Engineering, 2019, 183: 106361.

Wang, W., Wang, H., Su, Y., et al. Simulation of liquid flow transport in nanoscale porous media using lattice Boltzmann method. Journal of the Taiwan Institute of Chemical Engineers, 2021, 121: 128-138.

Wang, K., Yang, L., Yu, Y., et al. Influence of slip boundary on the hydrofoil with a curved slip boundary condition for the lattice Boltzmann method. Physics of Fluids, 2018, 30(12): 123601.

Wu, K., Chen, Z., Li, J., et al. Wettability effect on nanoconfined water flow. Proceedings of the National Academy of Sciences of the United States of America, 2017, 114(13): 3358-3363.

Yang, J., Boek, E. S. A comparison study of multi-component Lattice Boltzmann models for flow in porous media applications. Computers & Mathematics with Applications, 2013, 65(6): 882-890.

Yang, Y., Shan, M., Kan, X., et al. Thermodynamic of collapsing cavitation bubble investigated by pseudopotential and thermal MRT-LBM. Ultrasonics Sonochemistry, 2020, 62: 104873.

Yang, L., Yu, Y., Hou, G., et al. Boundary conditions with adjustable slip length for the lattice Boltzmann simulation of liquid flow. Computers & Fluids, 2018, 174: 200-212.

Zachariah, G. T., Panda, D., Surasani, V. K. Lattice Boltzmann simulations for invasion patterns during drying of capillary porous media. Chemical Engineering Science, 2019, 196: 310-323.

Zacharoudiou, I., Boek, E. S., Crawshaw, J. The impact of drainage displacement patterns and Haines jumps on CO_2 storage efficiency. Scientific Reports, 2018, 8(1): 15561.

Zhan, S., Su, Y., Jin, Z., et al. Study of liquid-liquid two-phase flow in hydrophilic nanochannels by molecular simulations and theoretical modeling. Chemical Engineering Journal, 2020, 395: 125053.

Zhang, T., Javadpour, F., Li, J., et al. Pore-scale perspective of gas/water two-phase flow in shale. SPE Journal, 2021, 26(2): 828-846.

Zhang, T., Javadpour, F., Yin, Y., et al. Upscaling water flow in composite nanoporous shale matrix using lattice Boltzmann method. Water Resources Research, 2020, 56(4): e2019WR026007.

Zhang, T., Li, X., Shi, J., et al. An apparent liquid permeability model of dual-wettability nanoporous media: A case study of shale. Chemical Engineering Science, 2018, 187: 280-291.

Zhang, T., Li, X., Sun, Z., et al. An analytical model for relative permeability in water-wet nanoporous media. Chemical Engineering Science, 2017a, 174: 1-12.

Zhang, Q., Su, Y., Wang, W., et al. Apparent permeability for liquid transport in nanopores of shale reservoirs: Coupling flow enhancement and near wall flow. International Journal of Heat and Mass Transfer, 2017b, 115: 224-234.

Zhang, C., Zhang, Q., Wang, W., et al. Capillary and viscous forces during CO_2 flooding in tight reservoirs. Capillarity, 2022, 5(6): 105-114.

Zhao, W., Jia, C., Zhang, T., et al. Effects of nanopore geometry on confined water flow: A view of lattice Boltzmann simulation. Chemical Engineering Science, 2021, 230: 116183.

Zhao, J., Kang, Q., Yao, J., et al. Lattice Boltzmann simulation of liquid flow in nanoporous media. International Journal of Heat and Mass Transfer, 2018, 125: 1131-1143.

Zhao, J., Liu, Y., Qin, F., et al. Pore-scale fluid flow simulation coupling lattice Boltzmann method and pore network model. Capillarity, 2023, 7(3): 41-46.